

Beam Corrections and Heterogeneous Arrays

II: Polarization

W. D. Cotton (NRAO,SARAO), T. Mauch (SARAO) June 7, 2021

Abstract—We present a technique for correcting the off-axis polarization artifacts arising from multiple antenna patterns in the same interferometer array and from asymmetries in a given antenna pattern. This technique was applied to simulated data sets for the MeerKAT+ array, MeerKAT plus 20 SKA design antennas. In one test using unpolarized sources, the level of instrumental linear polarization artifacts was reduced by a factor of 30 below the results using no correction. Correction of circular polarization was somewhat better.

A subsequent test was performed using polarized sources and the beam corrections applied resulted in image residuals approximately those obtained in the absence of beam asymmetries or differences in the antenna design. The recovered flux densities in Stokes I, Q, U and V well matched the values used in the simulations.

Index Terms—Antenna beam correction

I. INTRODUCTION

ASYMMETRIES in 2 axis alt-az mounted antennas introduce time dependent gain variations in the direction of sources off the axis as the antenna pattern rotates on the sky with parallactic angle. This is the equivalent of observing a time varying source and will introduce non-convolutional artifacts in the derived image. The use of heterogeneous arrays, arrays of antennas with dissimilar patterns on the sky, are an even more extreme case as the different antennas see a different effective sky even at the same time.

Antenna design can optimize polarization performance over only a limited area of the antenna beam on the sky. Away from this limited area, the antennas introduce a spurious polarized response to total intensity. As source fractional polarization can be a few percent or less, this instrumental response can dwarf source polarization in regions of the antenna pattern with comparable, or larger, instrumental polarizations. Observations over a range of parallactic angle (observing geometry) tends to reduce, but not eliminate this effect. This effect can render polarization measurements of limited use over a significant portion of the, otherwise useful, antenna beam. An array with heterogeneous antenna designs further complicate this problem.

Corrections in total intensity (Stokes I) were discussed in [1]. This memo describes a technique for also correcting instrumental polarization and presents tests using simulations of the heterogeneous array MeerKAT+ (MeerKAT plus SKA dishes) as implemented in the Obit package [2]¹.

National Radio Astronomy Observatory, 520 Edgemont Rd., Charlottesville, VA, 22903 USA email: bcotton@nrao.edu

South African Radio Astronomy Observatory, 2 Fir St., Observatory, South Africa

¹<http://www.cv.nrao.edu/~bcotton/Obit.html>

II. BEAM CORRECTIONS

Corrections to interferometer observations for the effects of the antenna patterns follows that outlined in [1]. A corrected Stokes I sky model is developed by a CLEAN based deconvolution that ignores the effects of the beam in making dirty/residual images but includes them in calculating the array's response to the sky model in each major cycle. In order to avoid numerical problems in regions of the image where the amplitude of the parallel hand antenna pattern is low, the ratio of the true antenna pattern to a “perfect” well behaved, symmetric, real beam is used to correct the CLEAN sky model to instrumental response. After multiple major cycles, the residuals approach zero and the sky model approaches the true sky model modified by the “perfect” antenna pattern.

This procedure can correct the spurious off-axis response to any I, Q, U or V but artifacts arising from Stokes I can seriously adversely affect the images of polarized emission so it is done first. The final Stokes I sky model can then be used to subtract the array's response from the initial dataset which is then used to image Q, U and V. This procedure is then repeated for Stokes Q, U and V, subtracting the response to the final CLEAN model before moving on to the next Stokes parameter.

For each component j of the sky model, the instrumental visibility response, R , is

$$R_{\nu,t,u,v,w}^j = \text{Beam}_{1,j,\nu,t} \text{Model}_{j,\nu,t} \text{Beam}_{2,j,\nu,t}^\dagger \quad (1)$$

where $\text{Beam}_{1,j,\nu,t}$ and $\text{Beam}_{2,j,\nu,t}$ are the complex antenna beam responses in the direction of component j at time t and frequency ν for the first and second antennas of the baseline; † signifies the conjugate transpose. The ratio of the true beam pattern for antenna k (1 or 2) to the “perfect” beam corresponding to the position of component j at frequency ν and time t is

$$\text{Beam}_{k,j,\nu,t} = \begin{bmatrix} X X_{k,j,\nu,t}^{\text{beam}} & X Y_{k,j,\nu,t}^{\text{beam}} \\ Y X_{k,j,\nu,t}^{\text{beam}} & Y Y_{k,j,\nu,t}^{\text{beam}} \end{bmatrix} \quad (2)$$

The variation in time is due to the parallactic angle change of alt-az mounted antennas tracking the source. The point visibility model for baseline p at time t and frequency ν for Stokes I is given by

$$\text{Model}_{p,\nu,t}^I = \begin{bmatrix} A_{j,\nu} e^{-i\theta} & 0 \\ 0 & A_{j,\nu} e^{-i\theta} \end{bmatrix} \quad (3)$$

with flux density $A_{j,\nu}$ and phase

$$\theta = -2\pi(u_{p,\nu,t} l_j + v_{p,\nu,t} m_j + w_{p,\nu,t} n_j), \quad (4)$$

l_j and m_j (with $n_j = \sqrt{1 - l_j^2 - m_j^2}$) are direction cosines. The visibility model for other Stokes parameters are given in the Appendix.

The response to the total model is the sum over all sky model components

$$R_{\nu,t,u,v,w}^{all} = \sum R_{\nu,t,u,v,w}^j. \quad (5)$$

Subtracting $R_{\nu,t,u,v,w}^{all}$ from the observed data will remove the response to the sky model including the spurious instrumental polarization terms.

III. OBIT IMPLEMENTATION

Beam corrections are implemented in the Obit Sky model class `ObitSkyModelVMBeamMF` and its parent `ObitSkyModelVMBeam`. These calculate the instrumental response to a sky model consisting of CLEAN components (points or Gaussians) and subtract (or divide) it from (into) the input visibility data. The beam corrections are based on a set of complex image cubes, finely spaced in frequency, for each of the 4 polarization products (XX,YY,XY,YX or RR,LL,RL,LR) for each antenna type to be corrected. For each parallactic angle, the beam values at the locations of each of the CLEAN components in the sky model being subtracted are interpolated in the appropriate frequency plane in each of the beam images, scaling in frequency if needed. For each sky model component, the instrumental response is then computed using Equation 2 followed by Equation 5 summing over all components. Visibility data are stored in time order so the arrays of beam gains only need to be updated when the parallactic angle changes sufficiently.

Since the calculation for each visibility is independent, multi-threading of this operation is very straightforward. A separate set of the arrays of interpolated beam values is needed for each thread. Currently, only a CPU version is available but a GPU version can be developed as needed. Several of the more expensive calculations, e.g. \sin/\cos , are implemented with SIMD vector instructions as available on the host CPU. Currently available are SSE, AVX, AVX2 and AVX512F.

In normal operations, the Obit routines that apply on-axis instrumental polarization corrections to linear basis data (XX,YY,XY,YX) also transform the data into a circular basis (RR,LL,RL,LR) as, until recently, this was required by the polarization imaging routines. When `MFBeam` operates on data in a linear basis (XX,YY,XY,YX) the output, model subtracted data is also in a linear basis. As no on-axis instrumental polarization calibration is needed, task `Lin2Cir` can be used for the transformation to a circular basis. The Obit imaging routines have been upgraded to image Q, U and V from linear basis data.

IV. SIMULATION TESTS

Test data were simulated as described in [1] which will include instrumental (spurious) polarized responses. Simulated data sets of unpolarized sources were imaged in Obit Task `MFBeam` as described in [1] to produce a corrected dataset. A subsequent test used simulations of polarized sources. A

comparison of images made with and without these corrections can be used to determine their efficacy.

Imaging was done on a Linux workstation running RHEL 7 with 16 x Intel(R) Xeon(R) CPU E5-2687W 0 @ 3.10GHz cores and 256 GByte of RAM, of which 100 GByte was configured into a RAM disk which was used for output and scratch files. This machine supports AVX but does not have a GPU.

A. Unpolarized Source Grid

The first simulation was of a grid of $3 \times 3 \sim 0.1$ Jy point sources separated by $20'$ with no noise or polarized emission. The simulation was of the MeerKAT+ array consisting of MeerKAT (diameter 13.5m) plus 20 outlying antennas of the SKA design (15m). This test dataset was used for Stokes I in [1]. The initial test used task `Lin2Cir` to convert the dataset to a circular basis (RR, LL, RL and LR) followed by `MFImage` imaging in Stokes I, Q, U and V. In this test no corrections were made for the simulated beams.

The second test first imaged and deconvolved the Stokes I with beam corrections using `MFBeam` as was done in [1]. This produces a data set from which the response to Stokes I, including spurious instrumental polarization, was subtracted from the input data. This corrected dataset was imaged using `Lin2Cir` and `MFImage`. A very light CLEAN was restricted to a radius of 5 pixels around the source position and CLEANing proceeded to a maximum 1000 components or a residual of $1 \mu\text{Jy/beam}$. Both tests used the same imaging parameters.

Cutouts around the sources imaged without beam corrections are shown in Figures 1 (Stokes Q), 3 (Stokes U) and 5 (Stokes V). These are to be compared with corrected images in Figures 2, 4 and 6 using much smaller stretches. As there was no polarized component in the model used to synthesize the data, all apparent Stokes Q, U and V in these figures is instrumental resulting from the antenna patterns used. More detail is given in Table I where for each of the sources shown in Figures 1–6, distance from the center, the peak Stokes I and the maximum and minimum values in the figures shown is given.

As a check, a simulation using the same source model but using a common, symmetric beam was imaged and, as expected, the polarized residuals are limited by the numerical noise from the computation.

B. One Hour Unpolarized Source Grid

The data in the test in Section IV-A extended over 12 hours for which each source response is averaged over much of the antenna pattern. As this will reduce the average instrumental polarization, a test using a shorter observation will be more representative of the effects on shorter observations. The test in Section IV-A was rerun using only one hour from the middle of the timerange; details of the results are given in Table II.

C. Polarized Source Grid

A second simulation similar to that discussed in Section IV-A was made but in which the sources in the grid used

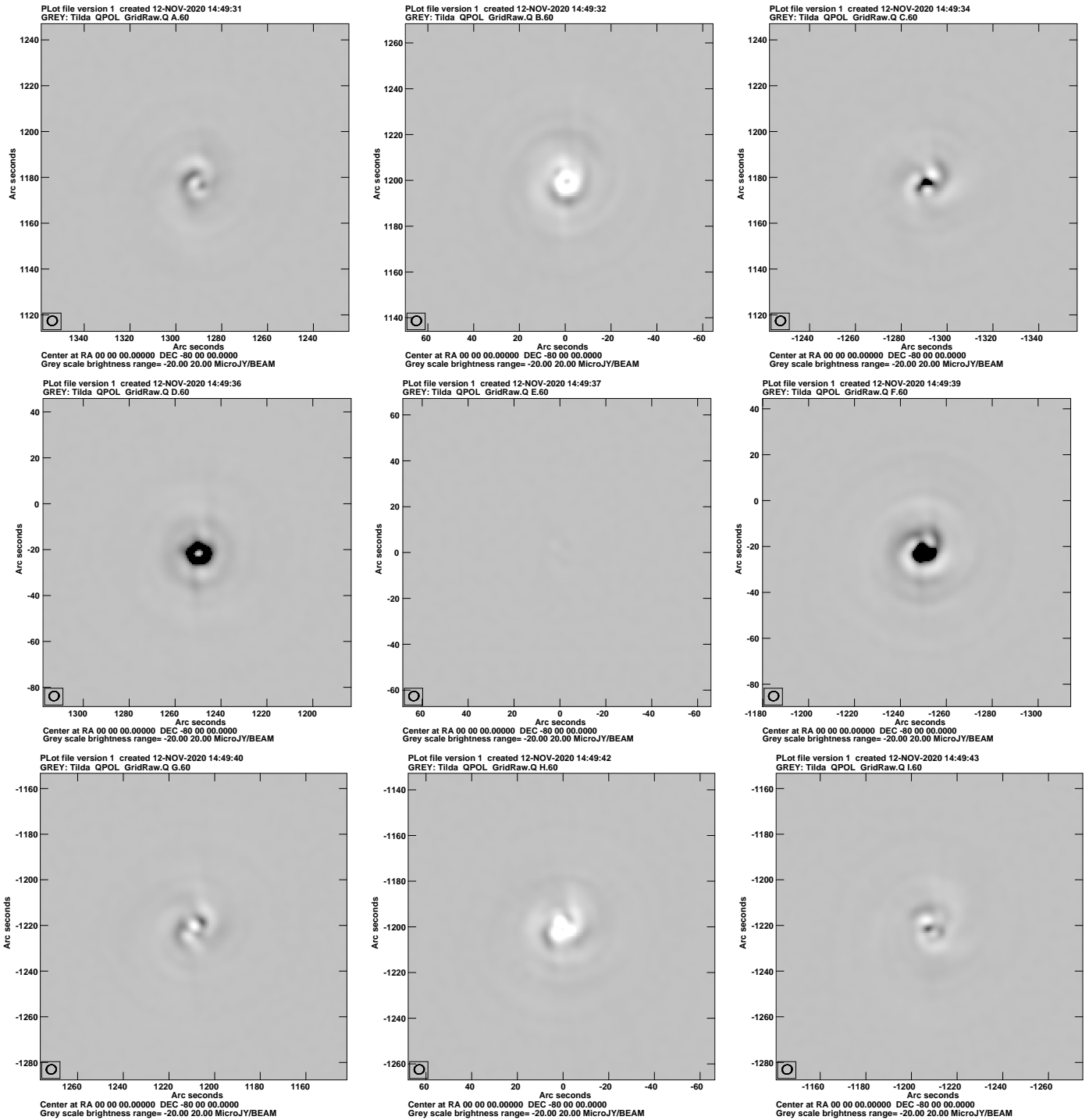


Fig. 1. Reverse gray scale of the Stokes Q in regions around the 9 simulated sources without correction for the Stokes I response. Top row has sources A, B and C, the middle row sources D, E and F and the bottom row G, H and I. The pixel range displayed is $-20 \mu\text{Jy}$ to $+20 \mu\text{Jy}$. RMS noise is $0.101 \mu\text{Jy/bm}$. The resolution is shown in the box in the lower left.

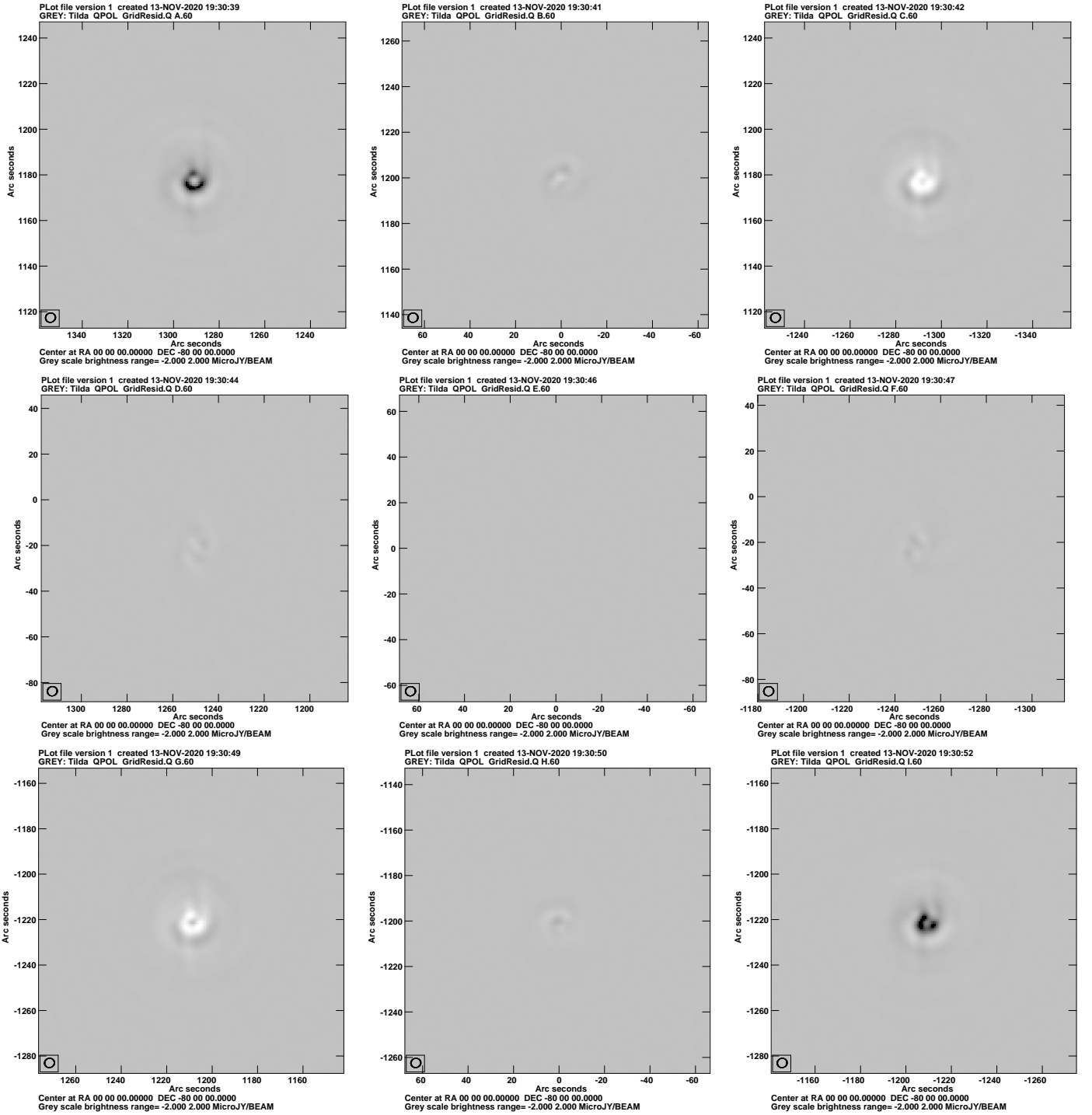


Fig. 2. Reverse gray scale of the Stokes Q in regions around the 9 simulated sources after correction for the Stokes I response. Compare to Figure 1. The pixel range displayed is $-2 \mu\text{Jy}$ to $+2 \mu\text{Jy}$, a factor of 10 lower than 1. RMS noise is 6.9 nJy/bm . The resolution is shown in the box in the lower left.

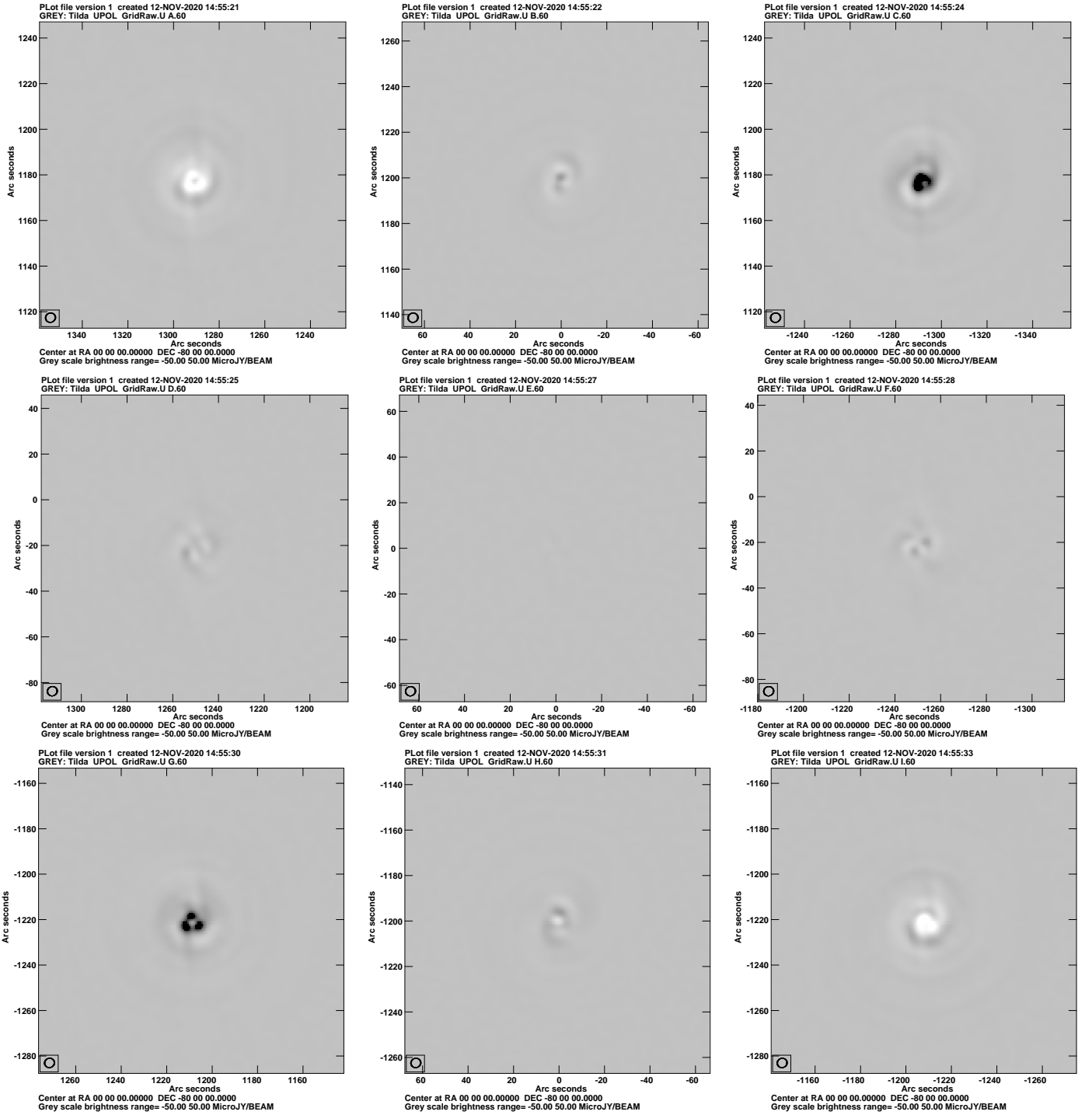


Fig. 3. Reverse gray scale of the Stokes U in regions around the 9 simulated sources without correcting for the Stokes I response. The pixel range displayed is $-50 \mu\text{Jy}$ to $+50 \mu\text{Jy}$. RMS noise is $0.128 \mu\text{Jy/bm}$. The resolution is shown in the box in the lower left.

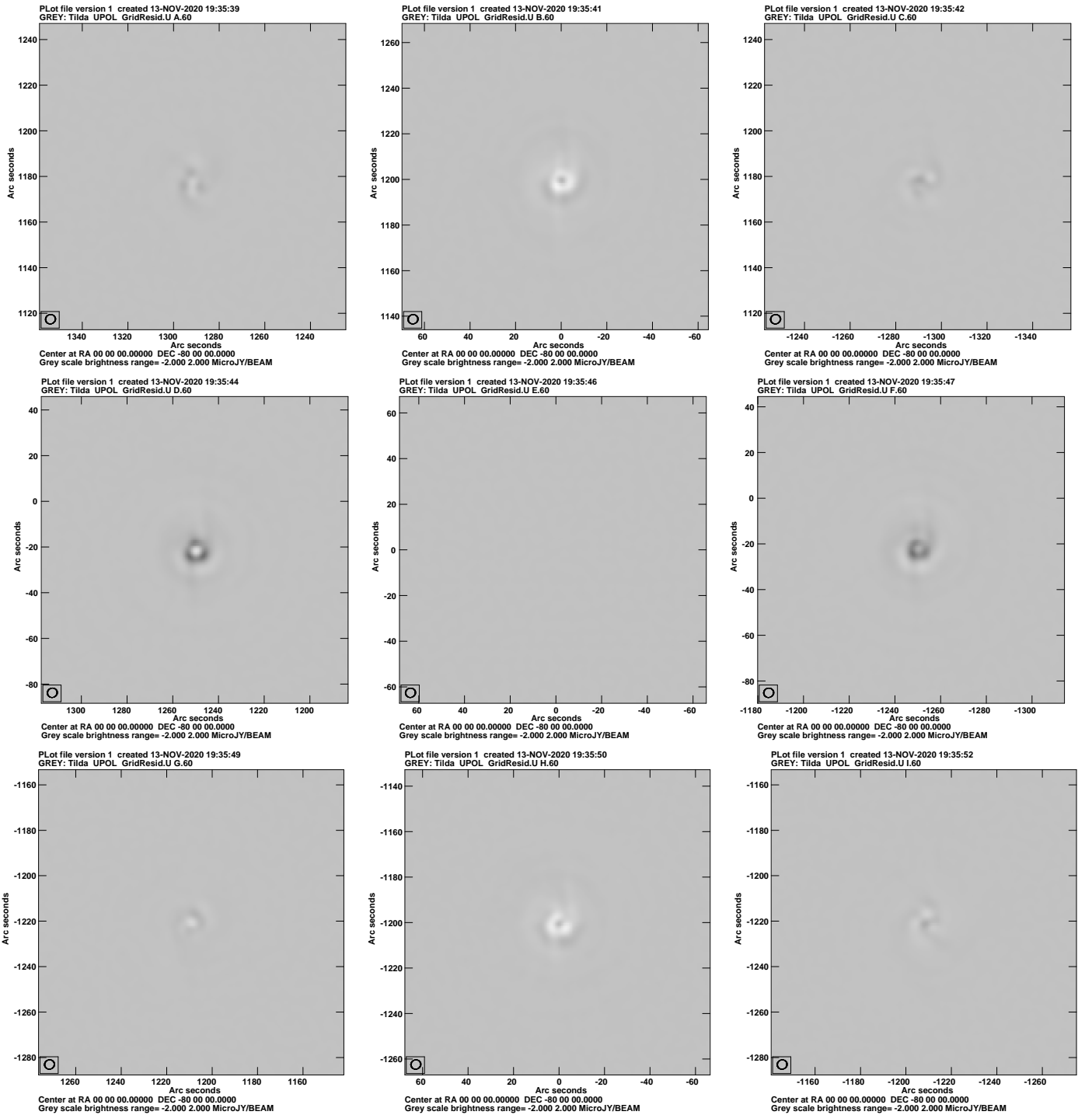


Fig. 4. Reverse gray scale of the Stokes U in regions around the 9 simulated sources after correction for the Stokes I response. Compare to Figure 3. The pixel range displayed is $-2 \mu\text{Jy}$ to $+2 \mu\text{Jy}$; a factor of 25 lower than Figure 3. RMS noise is 4.8 nJy/bm . The resolution is shown in the box in the lower left.

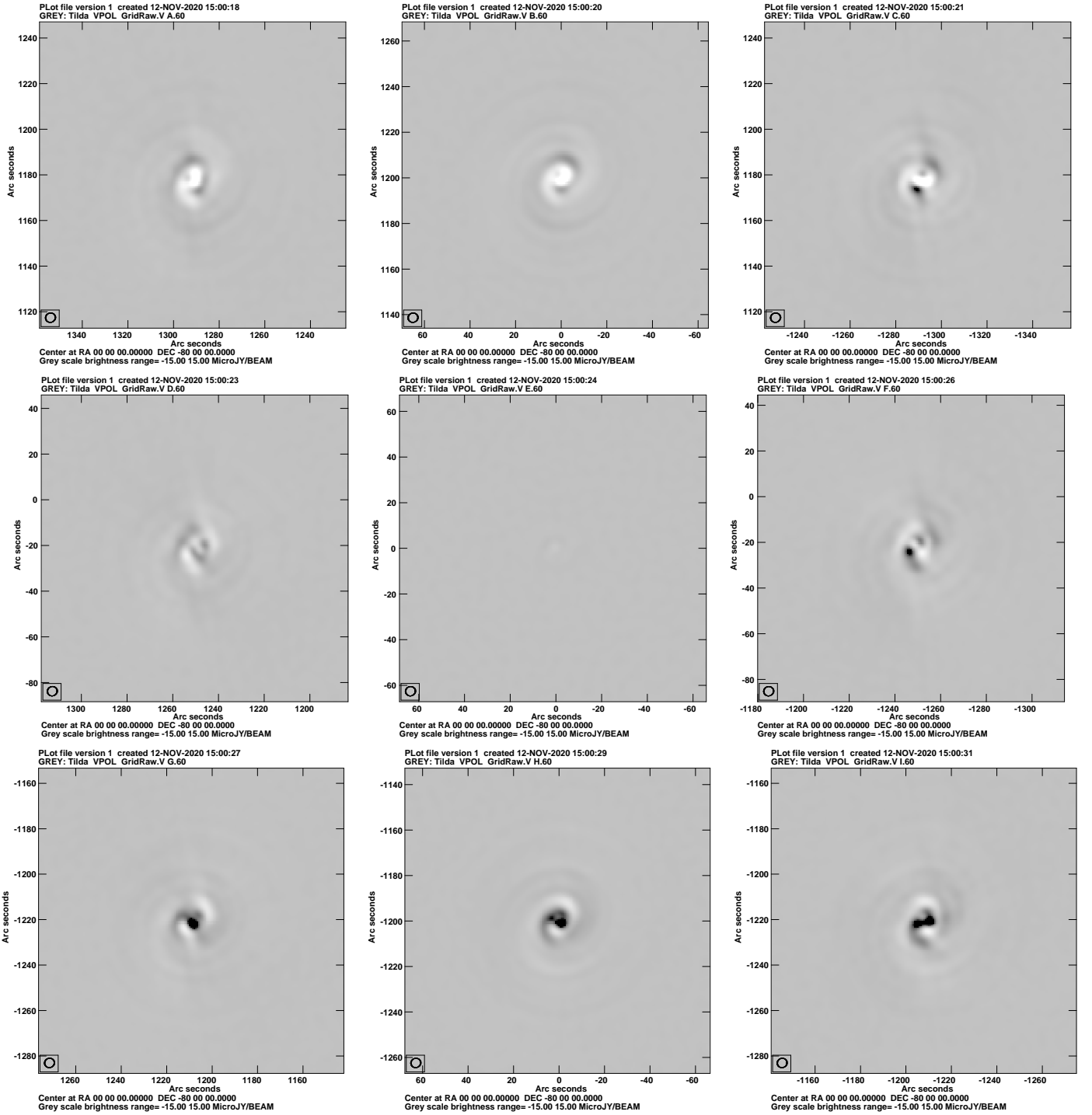


Fig. 5. Reverse gray scale of the Stokes V in regions around the 9 simulated sources without correction for the Stokes I response. The pixel range displayed is $-15 \mu\text{Jy}$ to $+15 \mu\text{Jy}$. RMS noise is $0.069 \mu\text{Jy/bm}$. The resolution is shown in the box in the lower left.

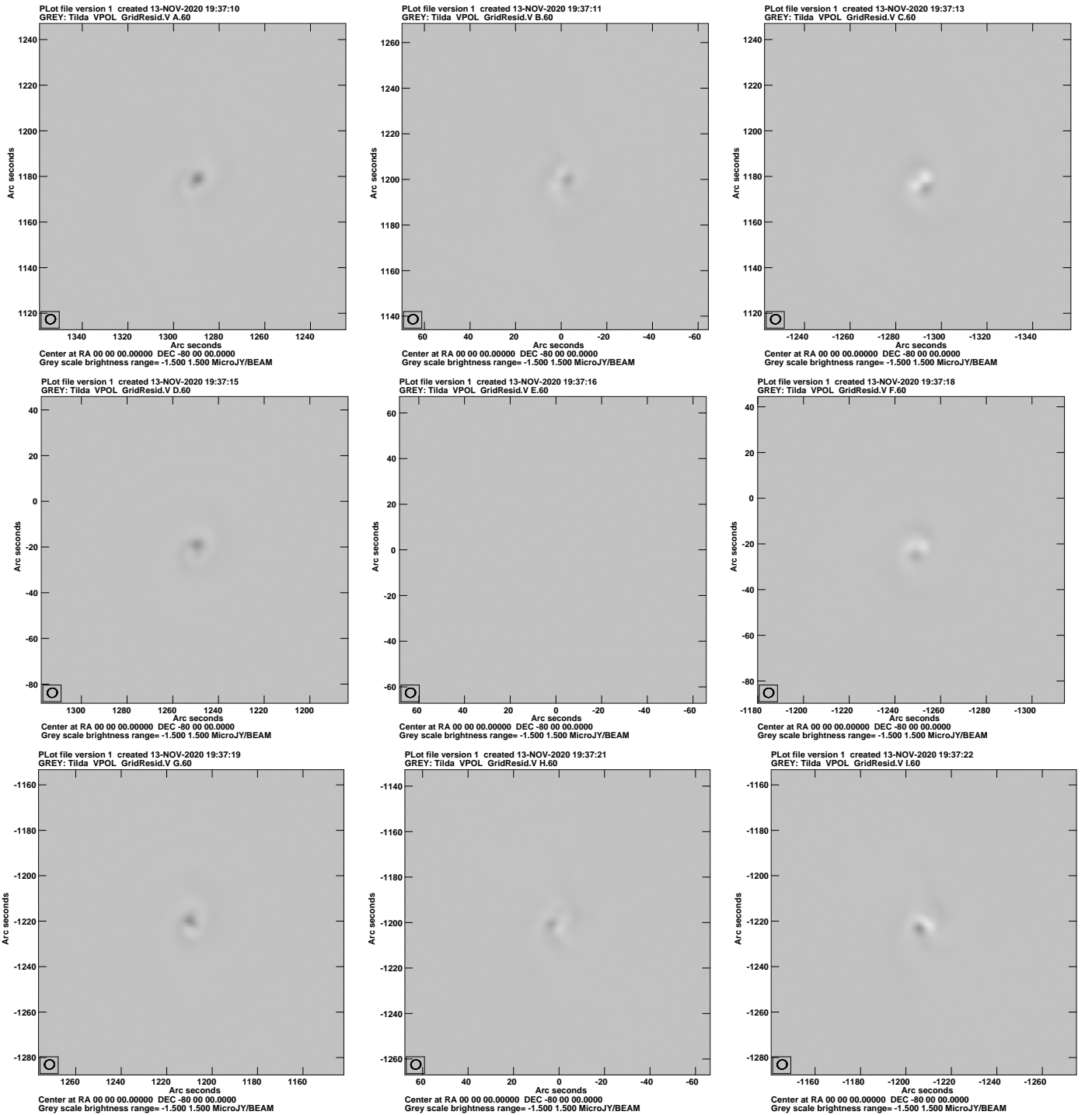


Fig. 6. Reverse gray scale of the Stokes V in regions around the 9 simulated sources after correction for the Stokes I response. Compare to Figure 5. The pixel range displayed is $-1.5 \mu\text{Jy}$ to $+1.5 \mu\text{Jy}$, a factor of 10 lower than 5. RMS noise is 2.0 nJy/bm . The resolution is shown in the box in the lower left.

TABLE I
UNPOLARIZED 12 HOUR GRID TEST

Source	dist	max I mJy/bm	Q_{uncorr} $\mu\text{Jy/bm}$	Q_{corr} $\mu\text{Jy/bm}$	U_{uncorr} $\mu\text{Jy/bm}$	U_{corr} $\mu\text{Jy/bm}$	V_{uncorr} $\mu\text{Jy/bm}$	V_{corr} $\mu\text{Jy/bm}$
A	44	56.3	13.9 -11.1	2.2 -0.4	9.1 -70.0	0.4 -0.3	7.1 -24.2	0.9 -0.1
B	30	70.9	9.0 -42.1	0.3 -0.4	21.1 -14.6	0.3 -1.5	6.8 -24.0	0.5 -0.3
C	44	56.2	29.3 -21.3	0.4 -2.4	84.7 -15.6	0.6 -0.3	16.8 -30.7	0.5 -0.8
D	31	70.9	39.4 -5.1	0.2 -0.2	14.1 -10.1	1.5 -0.8	7.0 -10.6	0.7 -0.1
E	0	94.3	1.0 -1.2	0.0 -0.0	1.7 -1.3	0.0 -0.0	0.5 -1.3	0.0 -0.0
F	31	72.0	51.2 -10.9	0.3 -0.2	14.4 -11.2	1.4 -0.3	17.9 -12.2	0.4 -0.6
G	43	55.6	16.5 -22.1	0.3 -2.1	68.8 -8.7	0.4 -0.6	30.1 -10.2	0.7 -0.2
H	30	74.6	8.6 -45.6	0.4 -0.2	20.8 -22.4	0.3 -1.4	26.6 -7.7	0.5 -0.3
I	43	57.0	17.4 -18.8	2.2 -0.4	13.6 -80.2	0.5 -0.4	30.4 -11.8	0.7 -0.8

Notes: Stokes Q, U and V uncorrected and corrected. Each column contains the maximum and minimum around each source.

TABLE II
UNPOLARIZED GRID 1 HOUR TEST

Source	dist	max I mJy/bm	Q_{uncorr} $\mu\text{Jy/bm}$	Q_{corr} $\mu\text{Jy/bm}$	U_{uncorr} $\mu\text{Jy/bm}$	U_{corr} $\mu\text{Jy/bm}$	V_{uncorr} $\mu\text{Jy/bm}$	V_{corr} $\mu\text{Jy/bm}$
A	44	56.3	33.5 -14.3	3.4 -1.2	47.9 -82.6	0.7 -0.4	15.7 -28.2	1.1 -0.5
B	30	70.9	20.9 -53.0	0.8 -1.1	35.7 -42.6	1.9 -2.3	21.4 -41.4	1.3 -0.2
C	44	56.2	75.9 -21.7	1.4 -3.8	102.1 -46.1	1.2 -0.9	24.0 -86.6	0.4 -1.0
D	31	70.9	61.8 -15.5	0.3 -0.1	12.3 -3.3	2.1 -2.6	1.3 -1.4	0.8 -1.0
E	0	94.3	1.3 -1.1	0.0 -0.0	3.6 -3.4	0.9 -0.8	1.3 -1.7	0.0 -0.0
F	31	72.0	104.5 -35.1	0.2 -0.1	4.8 -11.0	2.8 -1.5	3.6 -2.1	0.8 -2.5
G	43	55.6	30.4 -16.6	1.2 -3.4	76.3 -28.8	0.8 -0.7	27.9 -16.7	1.0 -0.4
H	30	74.6	19.4 -50.6	1.0 -0.8	47.5 -37.4	1.2 -2.2	40.4 -22.2	1.3 -0.2
I	42	57.0	69.6 -24.9	3.4 -1.3	61.1 -106.1	1.3 -0.3	85.6 -29.0	0.3 -0.7

Notes: Stokes Q, U and V uncorrected and corrected. Each column contains the maximum and minimum around each source.

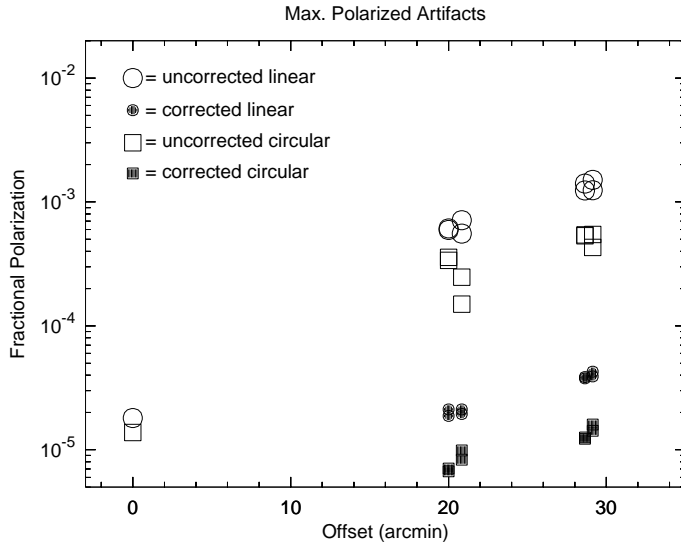


Fig. 7. Maximum fractional polarization artifacts as a function of distance from the pointing center near the sources shown in Figures 1-6 derived from Table I. Open circles and squares are the uncorrected linear and circular polarizations and the filled symbols are those after beam corrections.

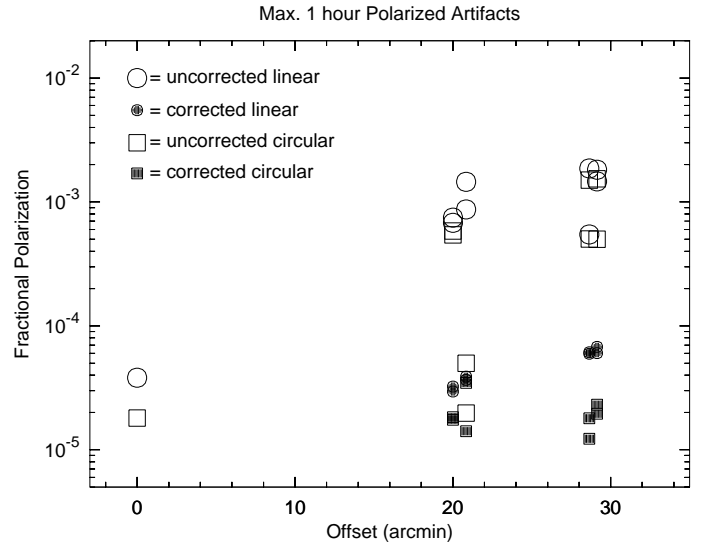


Fig. 8. Maximum fractional polarization artifacts as a function of distance from the pointing center near the sources shown in Figures 1-6 derived from Table II. This test used a one hour integration. Open circles and squares are the uncorrected linear and circular polarizations and the filled symbols are those after beam corrections.

had a polarized component. MFBeam and MFImage had been upgraded to image polarized emission from linear basis data so Lin2Cir was not needed. This test consists of 3 parts:

- **“Perfect” data**

The simulations used the same, symmetric beam patterns for all antennas. These should have no corruptions and were imaged by MFBeam using the symmetric beam

models used in the simulation. Residual artifacts are the results of the imaging rather than limitations of the beam corrections.

- **No correction**

These data used separate, asymmetric, MeerKAT and SKA beams and are corrupted by the beam effects. These

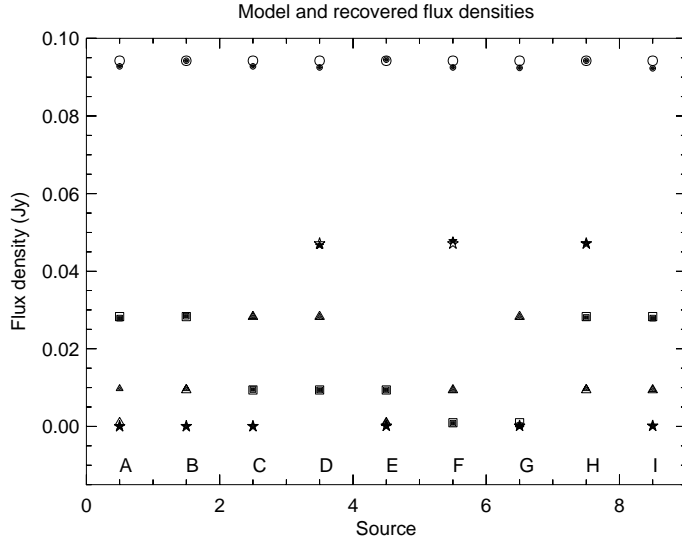


Fig. 12. Comparison of simulation model flux densities and those recovered from imaging. Sources are numbered A–I, open symbols are the input model and filled symbols are the values recovered from imaging. Stokes I is a circle, Stokes Q a square, Stokes U a triangle and Stokes V a star.

corruptions were ignored by imaging in MFImage.

• Beam correction

These corrupted data were also imaged in MFBeam with corrections in the order, Stokes I, Q, U and V.

Residual images of these three processings are shown in Figures 9–11 for all four Stokes parameters for a sample of sources. After MFBeam, the resultant images were primary beam corrected using the “perfect” beam shape and the fitted flux densities are compared with the model going into the simulation in Figure 12.

V. DISCUSSION

A. Unpolarized Source Grid Tests

Beam induced instrumental polarization results in artifacts at, and near, the location of total intensity features as is easily seen in Figures 1–6. The simulated sources are at three distances from the pointing center, those in the corners are at about the half power point in the beam mid-band. The locations of the sources well sample different orientations in the antenna pattern.

The ratios of the maximum linear and circular polarization artifacts in the vicinity of each source to the total intensity flux density shown in Table I is plotted in Figure 7. As expected, the maximum fractional polarization artifacts are very low near the pointing center and increase with increasing distance. The corrections applied in this test reduced the maximum linear artifacts by approximately a factor of 30 and somewhat more for circular polarization. The corrected results are at a much lower level than usually obtained on-axis by typical calibration.

In order to probe the residual instrumental polarization from a shorter observation than the 12 hours simulated in Section IV-A, the test was rerun with a one hour integration as described in Section IV-B. The comparison is given in Table II

and is plotted in Figure 8. Both the corrected and uncorrected peak polarization artifacts were approximately a factor of 2 higher than in the 12 hour test.

B. Polarized Source Grid Tests

The beam corrections reduced the image residual artifacts to about the level of the those with no beam corruptions as shown in Figures 9–11. Figure 12 shows that the input model flux densities in the various Stokes parameters are well recovered.

VI. CONCLUSIONS

At low frequencies and with small antennas, the field of view of radio interferometers is quite large and with the sensitivity of modern arrays sources can be detected out into the sidelobes of the antenna pattern where there are usually significant asymmetries in the antenna gain. For 2 axis antennas with alt-az mounts this pattern rotates on the sky causing apparent brightness variations in the sources. This causes artifacts in the images which are non convolutional and, if uncorrected, can limit the dynamic range of the image.

Furthermore, the spurious polarized instrumental response of the antennas increases with radius from the pointing direction and are also asymmetric. The spurious polarized response to Stokes I may corrupt, or even swamp, true polarized emission and this effect increases with distance from the pointing center. Rotation of the pattern with parallactic angle will tend to reduce the instrumental polarization but generally not eliminate it.

A technique for making wide area beam full polarization corrections is described and shown to be effective for full polarization imaging when used in a CLEAN like deconvolution. The general technique is to ignore beam effects when making dirty/residual images but then using an accurate beam model in computing the instrumental response to a partial sky model to be subtracted from the residual data before computing the next residual image. After multiple major cycles, the residual data converges towards zero and the accumulated sky model converges towards the correct one.

For wide area imaging a critical part of the technique is to to correct the instrumental response from the actual, poorly behaved one, to a well behaved, “perfect”, i.e. symmetric, one. This avoids amplifying the noise in parts of the image in which the primary beam is low but which contains strong sources needing to be included in the deconvolution. For an array using multiple antenna designs with multiple diameter antennas, using the “perfect” beam of the smaller antenna seems to give better results.

The tests described here are for the MeerKAT+ array under development which includes two antenna designs, 1) MeerKAT 13.5 m dishes and 2) SKA design, 15 m antennas. With the field of view and dynamic range requirements of this array and the very different antenna patterns, beam corrections will be needed all, or nearly all, of the time. This is an extreme case but a solution that works for it should also work for a homogeneous array with asymmetric antennas (which all are).

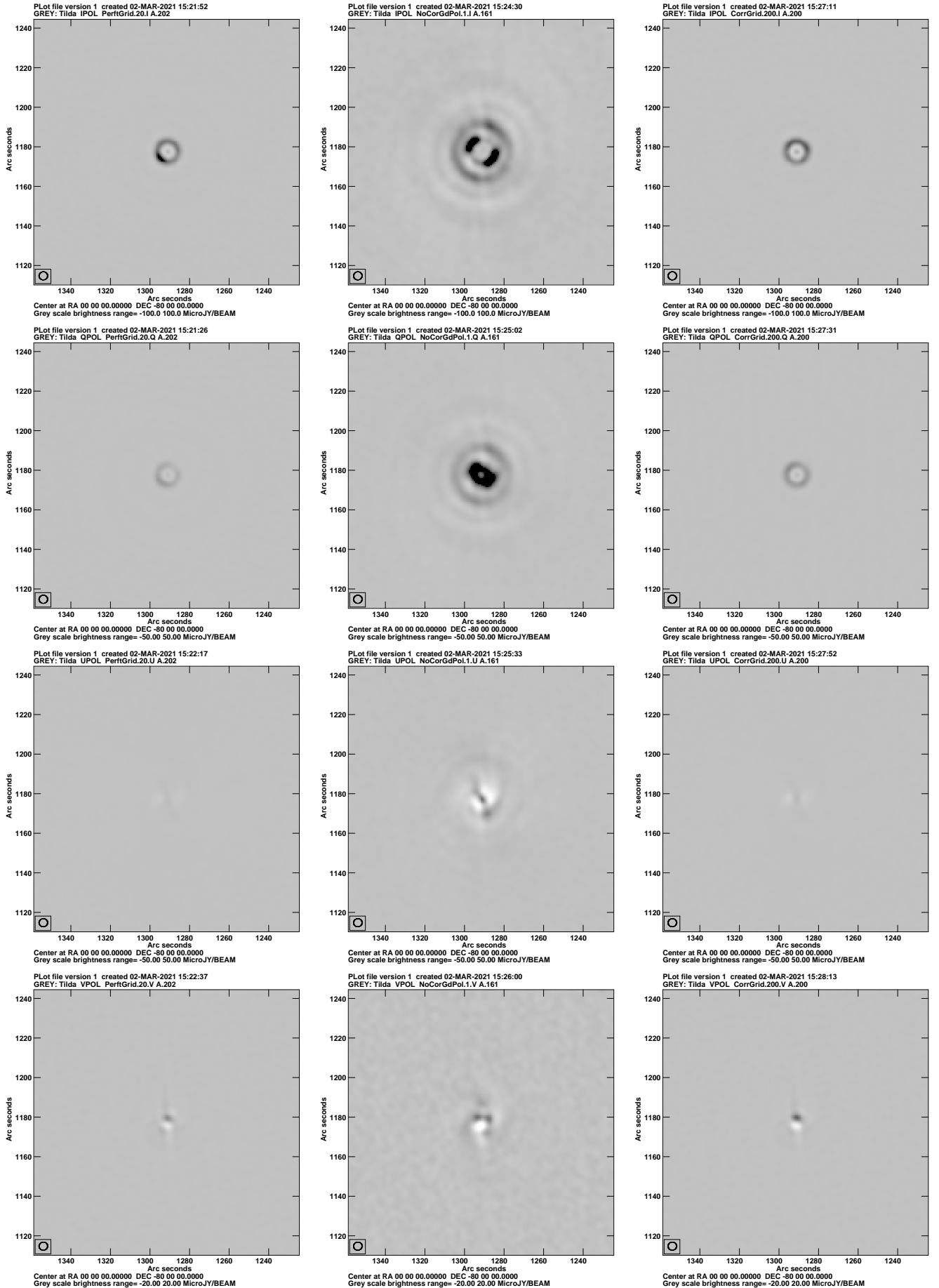


Fig. 9. Reverse gray scale of the residuals around source A. Left column is “Perfect” image, center column is without corrections and the right column is corrected. Top row is Stokes I, second row is Stokes Q, third row Stokes U and bottom row is Stokes V. The Stokes I pixel range displayed is $\pm 100 \mu\text{Jy}$, Stokes Q & U, $\pm 50 \mu\text{Jy}$, and for Stokes V $\pm 20 \mu\text{Jy}$. The resolution is shown in the box in the lower left.

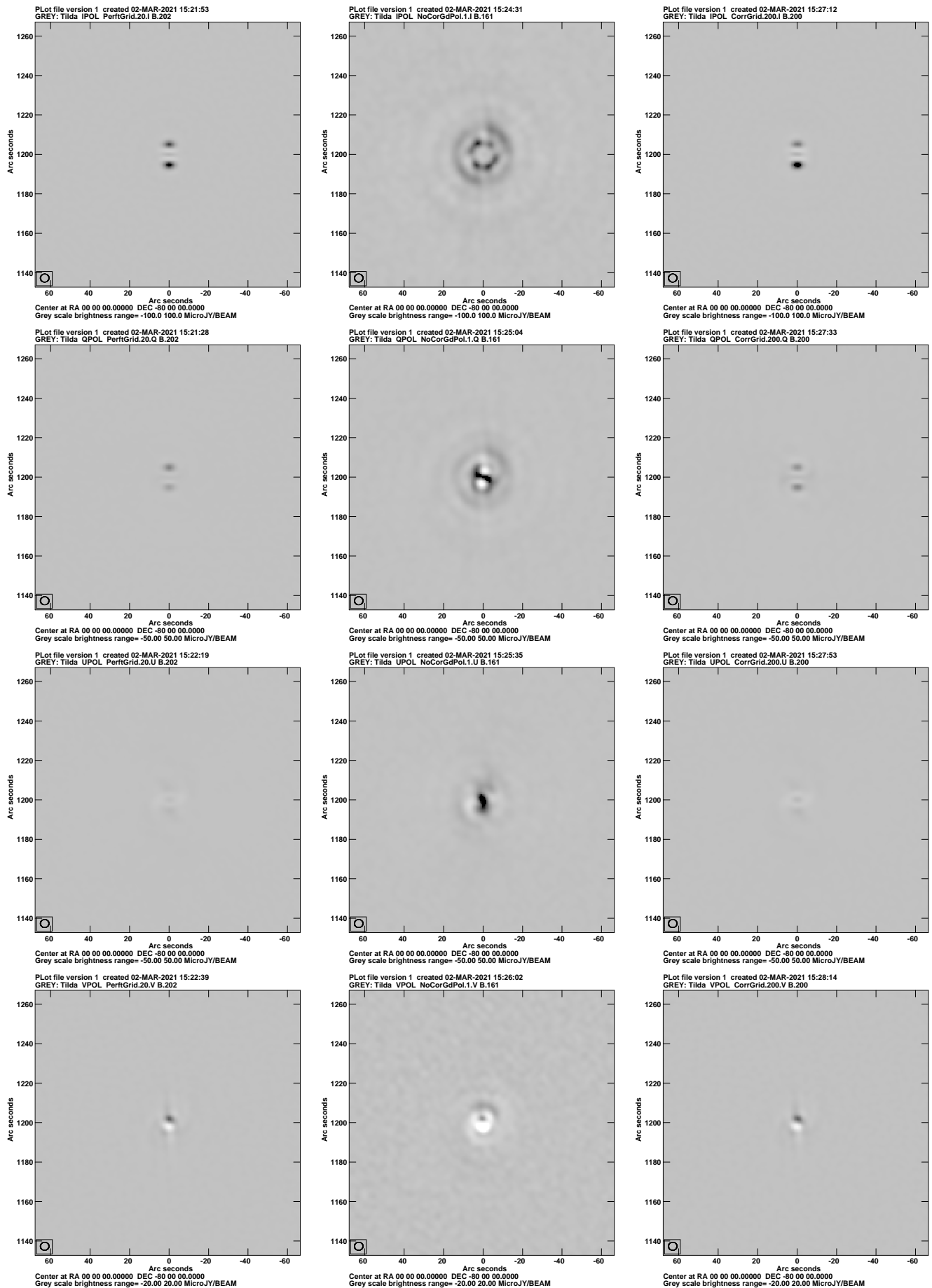


Fig. 10. Like Figure 9 but source B.

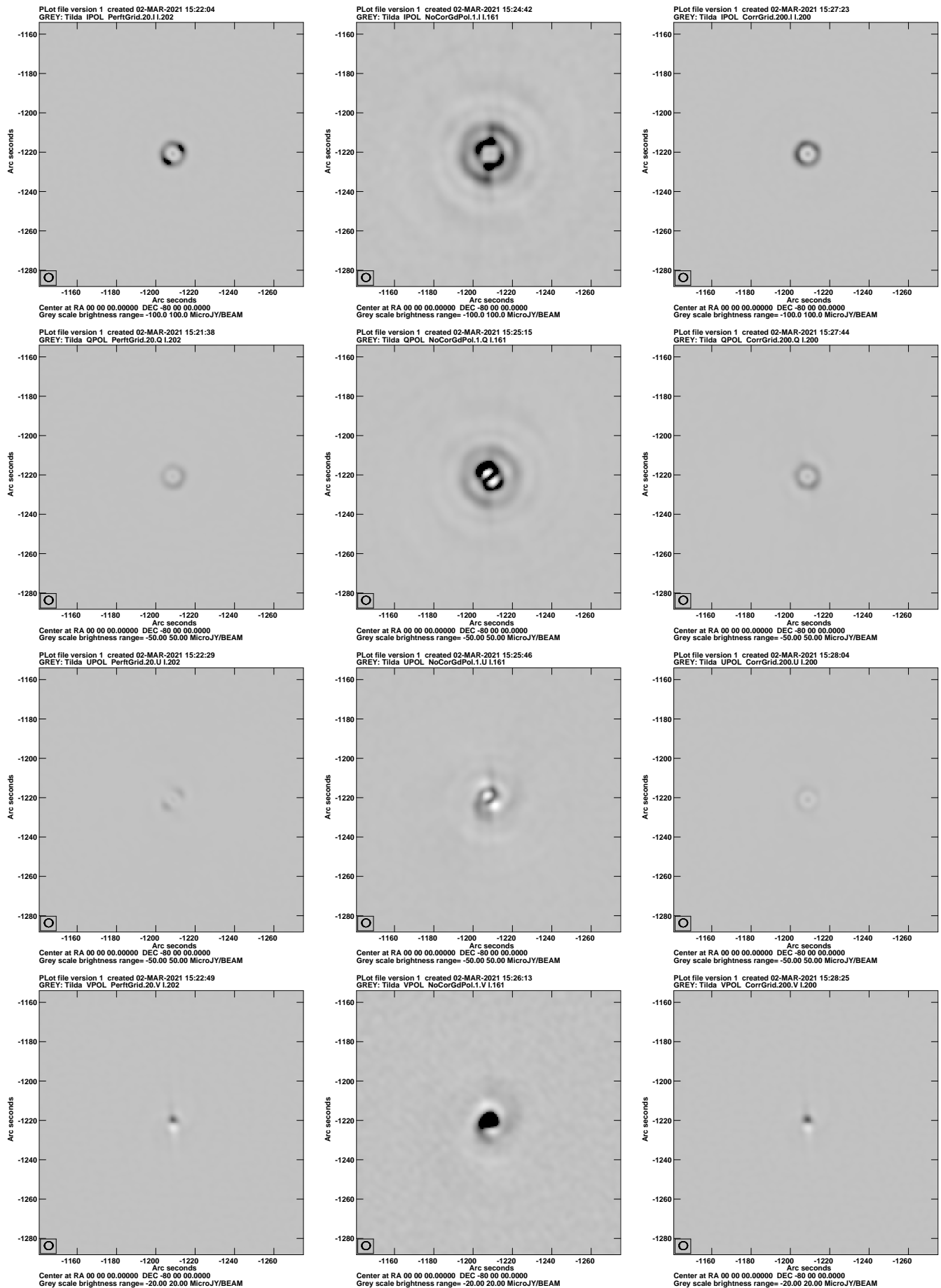


Fig. 11. Like Figure 9 but source I.

REFERENCES

- [1] W. Cotton and T. Mauch, “Beam Corrections and Heterogeneous Arrays I: Total Intensity,” *Obit Development Memo Series*, vol. 70, pp. 1–12, 2020.
- [2] W. D. Cotton, “Obit: A Development Environment for Astronomical Algorithms,” *PASP*, vol. 120, pp. 439–448, 2008.
- [3] A. R. Thompson, J. M. Moran, and G. W. Swenson, Jr., *Interferometry and Synthesis in Radio Astronomy, 2nd Edition*, Thompson, A. R., Moran, J. M., & Swenson, G. W., Jr., Ed. Wiley-Interscience, 2001.

APPENDIX

Following are the expressions for the model visibilities for Stokes I,Q,U and V models for both circular and linear feeds [3]. The variation in time is due to the parallactic angle change of alt-az mounted antennas tracking the source. These expressions are for point models for component j with amplitudes I,Q,U and V depending on the Stokes parameter; the visibility phase, θ for baseline p at time t and frequency ν is

$$\theta = -2\pi(u_{p,\nu,t}l_j + v_{p,\nu,t}m_j + w_{p,\nu,t}n_j), \quad (6)$$

where l_j and m_j (with $n_j = \sqrt{1 - l_j^2 - m_j^2}$) are direction cosines.

A. Circular Feeds

The following assume that the visibility data have had variations due the the parallactic angle removed in the calibration.

Stokes I model visibility:

$$Model_{p,\nu,t}^I = \begin{bmatrix} I_{j\nu}e^{-i\theta} & 0 \\ 0 & I_{j\nu}e^{-i\theta} \end{bmatrix} \quad (7)$$

Stokes Q model visibility:

$$Model_{p,\nu,t}^Q = \begin{bmatrix} 0 & -iQ_{j\nu}e^{-i\theta} \\ -iQ_{j\nu}e^{-i\theta} & 0 \end{bmatrix} \quad (8)$$

Stokes U model visibility:

$$Model_{p,\nu,t}^U = \begin{bmatrix} 0 & U_{j\nu}e^{-i\theta} \\ -U_{j\nu}e^{-i\theta} & 0 \end{bmatrix} \quad (9)$$

Stokes V model visibility:

$$Model_{p,\nu,t}^V = \begin{bmatrix} V_{j\nu}e^{-i\theta} & 0 \\ 0 & -V_{j\nu}e^{-i\theta} \end{bmatrix} \quad (10)$$

B. Linear Feeds

The cross hand correlations of linearly polarized feeds on alt-az mounter antennas depend on the parallactic angle, ψ :

$$\psi = \tan^{-1}\left(\frac{\cos \lambda \sin h}{\sin \lambda \cos \delta - \cos \lambda \sin \delta \cos h}\right) \quad (11)$$

where δ is the source declination, λ is the latitude of the antenna and h is the hour angle of the source.

Stokes I model visibility:

$$Model_{p,\nu,t}^I = \begin{bmatrix} I_{j\nu}e^{-i\theta} & 0 \\ 0 & I_{j\nu}e^{-i\theta} \end{bmatrix} \quad (12)$$

Stokes Q model visibility:

$$Model_{p,\nu,t}^Q = \begin{bmatrix} Q_{j\nu}\cos(2\psi)e^{-i\theta} & -Q_{j\nu}\sin(2\psi)e^{-i\theta} \\ -Q_{j\nu}\sin(2\psi)e^{-i\theta} & -Q_{j\nu}\cos(2\psi)e^{-i\theta} \end{bmatrix} \quad (13)$$

Stokes U model visibility:

$$Model_{p,\nu,t}^U = \begin{bmatrix} U_{j\nu}\sin(2\psi)e^{-i\theta} & -U_{j\nu}\cos(2\psi)e^{-i\theta} \\ -U_{j\nu}\cos(2\psi)e^{-i\theta} & -U_{j\nu}\sin(2\psi)e^{-i\theta} \end{bmatrix} \quad (14)$$

Stokes V model visibility:

$$Model_{p,\nu,t}^V = \begin{bmatrix} 0 & jV_{j\nu}e^{-i\theta} \\ -jV_{j\nu}e^{-i\theta} & 0 \end{bmatrix} \quad (15)$$